Solvation structure engineering with co-solvents enables tunable charge storage mechanisms in MXenes

Chaofan Chen, Albert de Kogel, Luca Bikker, Pranav Karanth, Hao Wang, Swapna Ganapathy, Marnix Wagemaker, Xuehang Wang [*]

Department of Radiation Science and Technology, Delft University of Technology, 2629 JB Delft, the Netherlands

ARTICLE INFO

ABSTRACT

Modulating ion-solvent interactions offers a powerful approach to tune the desolvation process, which in turn influences both the capacity and kinetics of electrochemical charge storage. This influence is particularly complex in 2D MXenes due to their surface redox activity and flexible interlayer spacing and thus remains under-explored. In this study, we investigate how tuning the Na^+ solvation structure using acetonitrile (ACN) co-solvents affects charge storage mechanism of $Ti_3C_2T_x$ MXene. The addition of ACN enables a new intercalation process at relatively positive potential, which enhances the overall capacitance by ~30 %. More interestingly, varying the ACN content leads to a transition in the charge storage mechanism of this additional process from non-Faradaic to redox-active. At lower ACN concentrations, strongly solvated Na^+ ions intercalate rapidly through a primarily non-Faradaic process, resulting in even better rate retention (72 % at 1 V s^{-1}) than in the pure aqueous electrolyte. Meanwhile, higher ACN content (>50 %) promotes ion desolvation, enabling distinct redox activity (confirmed by in-situ UV–vis) but reduces rate capability. These findings demonstrate a clear correlation between solvation structure and charge storage mechanism in 2D materials, offering a rational strategy to optimize performance via co-solvent design.

1. Introduction

As solar and wind energy become more widespread, stationary electrochemical storage systems are essential for grid stability [1]. Additionally, the rapid rise of portable electronics and electric vehicles is driving the development of energy storage technologies with both high energy and high power density. These requirements call for materials that combine large charge storage capacity, fast charge-discharge capability, and excellent cycling stability [2]. With a high surface-to-volume ratio and large interlayer spacing, two-dimensional (2D) materials possess favorable structure that allows easy access of ions to their extensive interlayer surface area with low resistance and helps maintain structural integrity during repeated cycling [3]. Among these, transition metal carbides and nitrides MXenes ($M_{n+1}X_nT_x$), particularly $Ti_3C_2T_x$, stand out due to their great mechanical strength, superior electrical conductivity, tunable surface chemistry, and good hydrophilicity [4–6].

MXenes have demonstrated superior charge storage performance in acidic and organic electrolytes, where fast surface redox reactions enable both high capacitance and excellent rate capability. However, safety concerns in these environments have motivated interests in neutral aqueous electrolytes [7], which offer milder, safer conditions but often suppress surface redox activity of MXene, resulting in moderate capacitance [8,9]. In dilute neutral aqueous electrolytes, cations such as Na^+ and Li^+ are strongly solvated, forming a tightly coordinated structure with four to six water molecules surrounding each ion. This strong coordination makes complete desolvation (or dehydration) difficult, leading to the frequent co-intercalation of water molecules with the ions in MXenes [10]. The co-inserted water molecules reduce interaction between the cation and MXene surface terminations, suppressing charge transfer [9]. As a result, charge storage in dilute neutral aqueous electrolytes is often dominated by electric double-layer (EDL) behavior, yielding relatively low capacitance [11].

Electrolyte modification has been explored as a powerful strategy to improve electrochemical performance for different neutral aqueous electrochemical energy storage systems, including aqueous Li-ion batteries, capacitors and zinc-metal batteries. Common approaches include increasing salt concentration, introducing molecular crowding agents

* Corresponding author.
  E-mail address: x.wang-22@tudelft.nl (X. Wang).

such as polyethylene glycol (PEG), or incorporating organic co-solvents [11–13]. These strategies not only suppress water activity and expand the electrochemical stability window but also reshape the solvation structure, which in turn influences the charge storage behavior [14].

Modifying solvation structure has also been shown to alter ion intercalation behavior and affect the charge storage for MXene electrodes [15]. For example, both water-in-salt (WIS) and molecular crowding electrolytes (MCEs) can enable additional intercalation steps into MXenes' interlayer at relatively high potentials, contributing to extra capacity [16,17]. In MCEs, modified Li^+ hydration promotes a new intercalation step at −0.25 V, involving the insertion of strongly solvated Li^+ ions, possibly along with PEG molecules, leading to ~25 % higher capacitance compared to dilute electrolytes [17]. In 19.8 m LiCl WIS electrolytes, Li^+ ions are coordinated with ~2.85 water molecules, which favors direct intercalation at more positive potentials without prior desolvation [16,18]. This desolvation-free intercalation involves minimal charge transfer, causes a sharp 1.9 Å increase in interlayer spacing, and contributes to enhanced capacitance. Compared to WIS and MCEs, whose high viscosities significantly reduce ionic conductivity, introducing organic co-solvents into aqueous electrolytes has emerged as an effective strategy to tune ion solvation while preserving sufficient ionic transport. Acetonitrile (ACN), with its low viscosity (~0.37 cP), and moderate dielectric constant (~37.5), can efficiently disrupt the water-water hydrogen bonding network and modulate cation solvation through ion-dipole interactions [19,20]. This solvation tuning has been shown to suppress parasitic water decomposition reactions and inhibit dendrite formation in zinc-metal batteries, highlighting ACN's potential to enhance interfacial stability and electrochemical performance in aqueous energy storage systems [21–23]. However, the impact of ACN as a co-solvent on ion intercalation in MXenes remains to be systematically understood.

In our study, we reveal how systematically tuning the Na^+ solvation structure using ACN-water hybrid electrolytes can regulate ion intercalation and charge storage mechanisms of MXenes. Interestingly, the introduction of ACN activates an additional ion intercalation step (S1 or S1') at more positive potentials (Fig. 1, middle & right panel) beyond the typical ion intercalation (S2) (Fig. 1, left panel). As the ACN content increases, nuclear magnetic resonance (NMR) and Fourier transform infrared (FTIR) spectroscopy confirm a progressive weakening of Na^+-H_2O interaction with increasing ACN content. This change modulates the nature of high-potential intercalation (S1 or S1'), shifting from a non-faradaic process at low ACN concentration (Fig. 1, middle panel) to a pseudocapacitive mechanism at higher concentrations (Fig. 1, right panel). Specifically, in 75 H_2O:25 ACN electrolyte, additional intercalation of solvated Na^+-H_2O clusters occurs with rapid kinetics, resulting in a ~30 % increase in capacitance along with superior rate capability, retaining 72 % of the capacitance at 1 V s^{-1} compared to 62 % in pure water. Our findings offer fundamental insights into the charge storage process in co-solvent systems and provide guidance for the rational design of electrolytes to enhance the energy storage performance of 2D material-based electrodes.

2. Results and discussions

2.1. Electrochemical behavior of $Ti_3C_2T_x$ in ACN-containing electrolytes

The $Ti_3C_2T_x$ MXene synthesized by in-situ HF etching method exhibited the characteristic (0 0 l) reflections in its X-ray diffraction (XRD) pattern (Figure S1a) and a layered morphology (Figure S1b), confirming its well-preserved lamellar structure. To investigate the influence of ion solvation on the electrochemical performance of $Ti_3C_2T_x$ MXene, the $NaClO_4$ was selected as the salt due to its exceptionally high solubility in both water and ACN. This enables systematic exploration over a wide solvent composition range, unlike NaCl, which shows salting-out effect in ACN-rich media. 2 M $NaClO_4$ electrolytes with varying H_2O:ACN volume ratios were prepared and are denoted as 2 M $NaClO_4$ x H_2O: y ACN, where x, y represents the respective volume parts of H_2O and ACN, respectively).

Cyclic voltammetry measurements were conducted in a three-electrode configuration using $Ti_3C_2T_x$ as the working electrode, activated carbon as the counter electrode, and an Ag wire as the reference electrode in H_2O:ACN hybrid electrolytes. In 2 M $NaClO_4$ H_2O, $Ti_3C_2T_x$ exhibited a nearly rectangular cyclic voltammogram (CV) shape from −1.1 V to 0 V vs. Ag (Fig. 2a), characteristic of EDL behavior. Upon
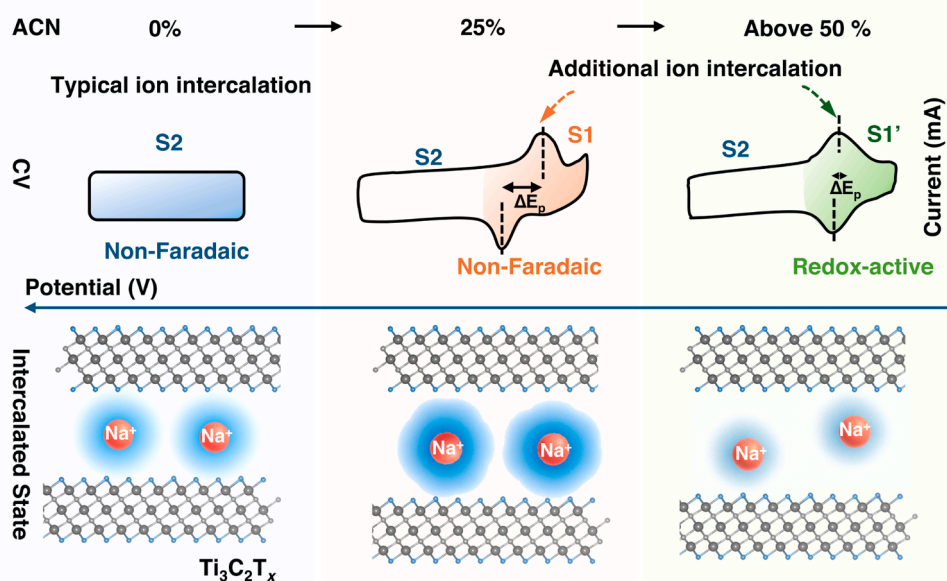
Fig. 1. Schematic illustration showing cyclic voltammograms (CVs) and corresponding charge storage mechanisms of $Ti_3C_2T_x$ MXene in 2 M $NaClO_4$ aqueous electrolytes with varying ACN content: pure H_2O (left panel), 25 % ACN (middle panel), and above 50 % (right panel). Red spheres represent Na^+ ions, each surrounded by a blue, diffuse layer denoting the solvation shell. Grey, silver, and blue spheres represent Ti, C, and O atoms in the MXene layers, respectively. Incorporation of ACN introduces a distinct high-potential intercalation step (S1/S1') alongside the typical ion intercalation process (S2). In 75 H_2O:25 ACN, this new step proceeds through intercalation of strongly solvated Na^+-H_2O species without significant charge transfer (non-Faradaic). In 50 H_2O:50 ACN, weaker interaction between Na^+ and H_2O facilitates Na^+ desolvation, leading to redox-active process (S1').

Fig. 2. Electrochemical behavior of $Ti_3C_2T_x$ MXene (a) Cyclic voltammograms (CV) of $Ti_3C_2T_x$ in different 2 M $NaClO_4$ H_2O: ACN electrolytes at 5 mV s^{-1}. CV of $Ti_3C_2T_x$ in 2 M 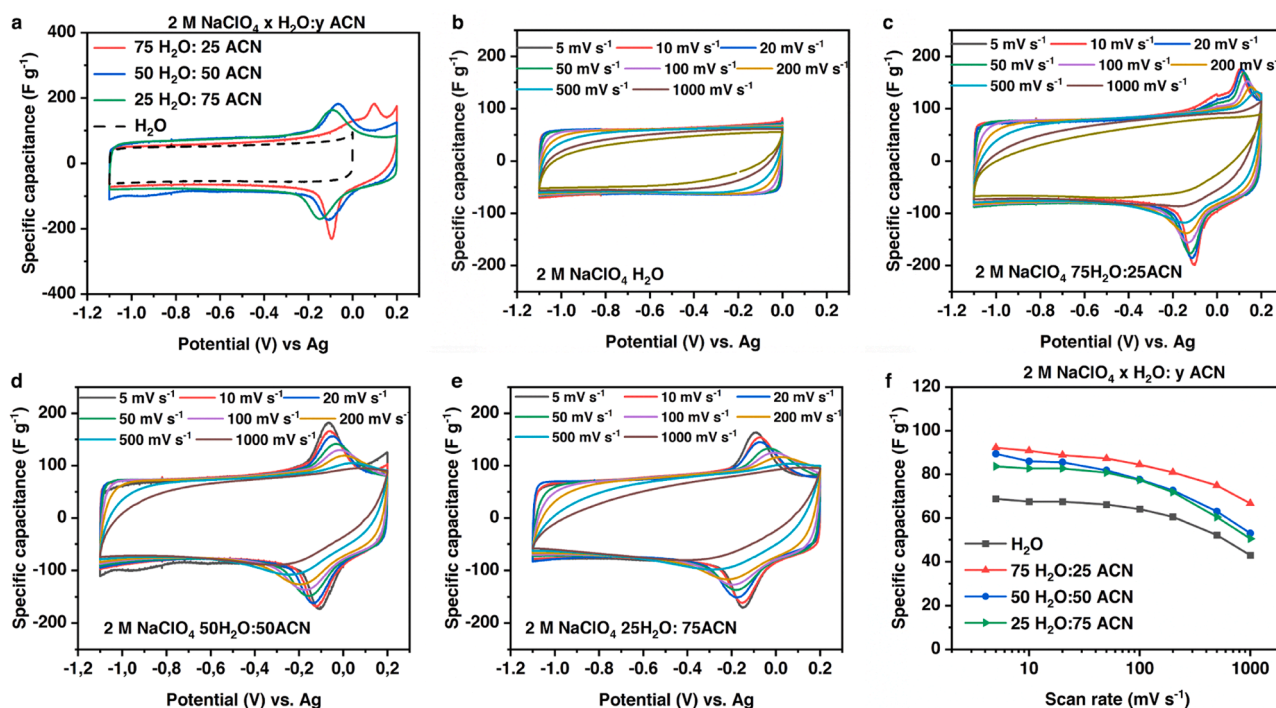$NaClO_4$ in (b) H_2O. (c) 75 H_2O:25 ACN. and (d) 50 H_2O:50 ACN. (e) 25 H_2O:75 ACN at different scan rates ranging from 5 mV s^{-1} to 1 V s^{-1}. and (f) Rate performance in 2 M $NaClO_4$ H_2O:ACN electrolytes.

introducing ACN as the co-solvent, the electrochemical response changed markedly (Fig. 2a). The applicable voltage window of $Ti_3C_2T_x$ improves with increasing ACN content, as evidenced by a lower steady-state leakage current measured at 0.2 V vs. Ag (**Figure S2**). This improvement is attributed to reduced free water reactivity and suppressed oxidative degradation of MXene. Notably, distinct redox peaks emerged in ACN-containing electrolytes, which were absent in pure aqueous electrolytes. In 75 H_2O:25 ACN, a sharp cathodic peak appeared at −0.09 V, accompanied by an anodic peak at +0.1 V, yielding a peak separation (ΔE_p) of 0.19 V at 5 mV s^{-1} (Fig. 2a). In 50 H_2O:50 ACN, the CV curve became more symmetric, with a broader and less intense cathodic peak at −0.11 V and a reduced ΔE_p of 0.03 V. The capacity contribution of the redox peaks (S1 or S1') in the CV was estimated by subtracting the baseline contribution, approximated as a rectangular area using the current at −0.3 V, from the total integrated area under the CV curve. Based on this method, the peaks contribute to 35 % and 30 % of the overall capacity in 75 H_2O:25 ACN and 50 H_2O:50 ACN electrolytes, respectively. Importantly, the differences in peak shape and ΔE_p indicate that the charge storage mechanisms at the corresponding peak potentials differ between the 75:25 and 50:50 electrolytes. Further increasing the ACN content to 75 % merely shifted the redox peaks negatively to −0.15 V, with minimal change in CV shape or peak intensity. These electrochemical features differ significantly from those observed in pure ACN. In 2 M $NaClO_4$ ACN, $Ti_3C_2T_x$ electrode exhibits a much wider stability window and broad, nearly symmetric peaks centered at −0.5 V, while no characteristic peaks appear in the positive potential region (**Figure S3**). This behavior is consistent with the partially (de-)intercalative process previously reported for Li$^+$ ions in ACN-based systems [15] and is accompanied by a lower capacitance and poorer rate performance.

Galvanostatic charge-discharge (GCD) measurements further confirmed these findings (**Figure S4**). In 2 M $NaClO_4$ H_2O, the GCD curve displayed a nearly triangular shape, consistent with rectangular CV profiles. In 75 H_2O:25 ACN, the GCD curve became asymmetric with sloped plateau. In contrast, more symmetric GCDs with short plateaus

were observed in 50 H_2O:50 ACN and 25 H_2O:75 ACN, consistent with the peaks featured in the corresponding CV curves. To examine the university of this solvent-dependent behavior, the charge storage behavior of $Ti_3C_2T_x$ electrodes was tested in 2 M $LiClO_4$ and 2 M Mg $(ClO_4)_2$ dissolved in a 75 H_2O:25 ACN mixture (**Figure S5**). In both electrolytes, similar cathodic features were observed, indicating that solvation-modulated intercalation is not unique to Na$^+$. However, the corresponding anodic peaks were largely absent, likely because the de-intercalation of solvated Li$^+$/Mg^{2+} occurs at potentials where $Ti_3C_2T_x$ begins to oxidize, resulting in poor reversibility.

To evaluate the rate performance, CV scans were performed from 5 to 1000 mV s^{-1} (Fig. 2b-2e). Notably, the peak features remained visible up to 500 mV s^{-1} for all ACN-containing electrolytes. Importantly, an enhancement in gravimetric specific capacitance was observed by introducing ACN as co-solvent at any scan rates due to the additional electrochemical process. At 5 mV s^{-1}, the capacitance increased from 68.8 F g^{-1} in H_2O, to 82.7 F g^{-1} in 25 H_2O:75 ACN, 89.4 F g^{-1} in 50 H_2O:50 ACN, and 92.3 F g^{-1} in 75 H_2O:25 ACN (Fig. 2f). Notably, best rate performance was also delivered in 75 H_2O:25 ACN electrolyte, achieving 66.6 F g^{-1} (72 % retention) at 1000 mV s^{-1}, outperforming H_2O (42.9 F g^{-1}, 62 %), 50 H_2O:50 ACN (52.9 F g^{-1}, 59 %), and 25 H_2O:75ACN (50.5 F g^{-1}, 61 %) electrolytes. Given the similar electrochemical features in 50 H_2O:50 ACN and 25 H_2O:75 ACN electrolytes, further analysis only focused on H_2O, 75 H_2O:25 ACN, and 50 H_2O:50 ACN electrolytes.

To elucidate the nature of the additional process, charge storage kinetics were evaluated by analyzing the slope of log(i)-log(v) plots (b-value) at cathodic peak potential [24]. The extracted b-values were 0.85, and 0.8 for 75 H_2O:25 ACN and 50 H_2O:50 ACN, respectively (Fig. 3a), suggesting this process was dominated by surface-controlled behavior. In comparison, a b-value of 0.95 was obtained in 2 M $NaClO_4$ H_2O, where the peak feature is absent, indicative of ideal capacitive behavior. To further distinguish between surface and diffusion-controlled contributions, the current response was analyzed using Dunn's method, where the measured current i(V) at a given potential is expressed as the sum of
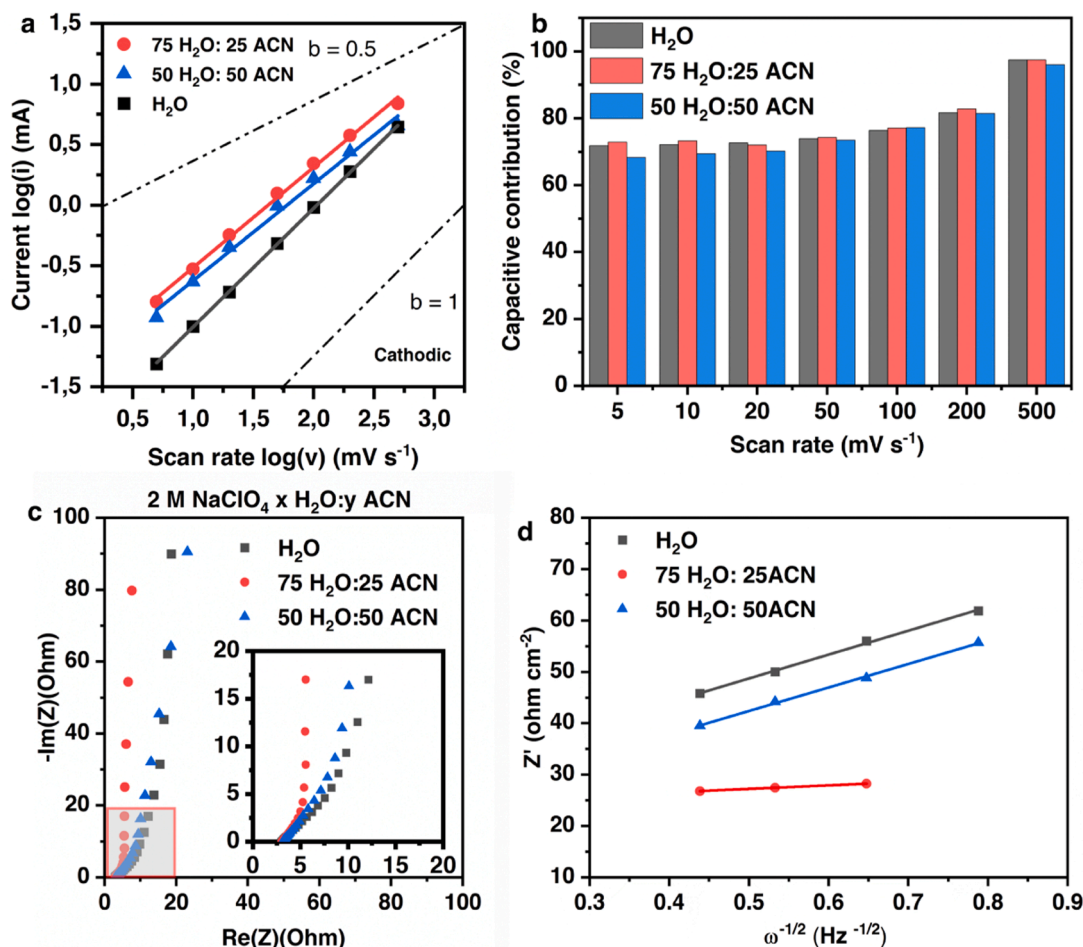
Fig. 3. Charge storage kinetics of $Ti_3C_2T_x$ in 2 M $NaClO_4$ H_2O, 75 H_2O:25 ACN and 50 H_2O:50 ACN. (a) Linear fitting of logarithm of cathodic peak currents log(i) versus the logarithm of scan rates log(v) for $Ti_3C_2T_x$. (b) Surface-contributed capacitance contribution at different scan rates. (c) Nyquist plots of $Ti_3C_2T_x$ at open circuit voltage. (d) Linear fit of real impedance (Z') versus the inverse square root of angular frequency ($\omega^{-1/2}$) in the Warburg frequency region.

a capacitive contribution k_1v and a diffusion-controlled contribution $k_2v^{1/2}$ [25]. Using this approach, the surface-controlled (capacitive) contribution at 500 mV s^{-1} was determined to be 97.5 % for both H_2O and 75 H_2O:25 ACN, and 96.1 % for 50 H_2O:50 ACN (Fig. 3b). Electrochemical impedance spectroscopy (EIS) further confirmed the capacitive-dominated behavior, showing nearly vertical slopes in the low-frequency region of Nyquist plots (Fig. 3c). Among them, the steepest low-frequency slope was shown in 75 H_2O:25 ACN, while 50 H_2O:50 ACN showed the shallowest slope and the lowest phase angle at 0.01 Hz in Bode plots (**Figure S6**), suggesting slower kinetics at higher ACN content. A magnified view of the high-frequency region showed no clear semicircle, indicating negligible charge-transfer resistance in all electrolytes (Fig. 3c). To study the ion transport kinetics further, the Warburg coefficient (σ) was extracted from the linear region of real impedance Z' versus $\omega^{-1/2}$ [26]. The lowest σ was obtained for 2 M 75 H_2O:25 ACN (6.8 Ω cm^{-2} s$^{1/2}$) compared to H_2O (45.7 Ω cm^{-2} s$^{1/2}$) and 50 H_2O:50 ACN (46.5 Ω cm^{-2} s$^{1/2}$), indicating faster ion diffusion in $Ti_3C_2T_x$ within 75 H_2O:25 ACN electrolytes (Fig. 3d). Therefore, while the additional electrochemical process in ACN-containing electrolytes remain surface-controlled, their charge transport kinetics depend on ACN content. Despite the large ΔE_p in 75 H_2O:25 ACN, the process (S1) exhibits high capacitive contribution and fastest kinetic, indicating that the peak separation arises from a distinct intercalation mechanism rather than sluggish ion diffusion. In contrast, 50 H_2O:50 ACN shows more symmetric redox peaks (S1') but exhibits slower kinetic.

2.2. Tunable charge storage mechanisms at different ACN ratio: from non-Faradaic to redox-active

To gain a deeper insight into the charge storage mechanisms underlying the additional electrochemical process, operando ultraviolet-visible (UV–Vis) spectroscopy was conducted during electrochemical cycling. This method tracks variations in light absorbance as a function of applied potential, which reflects changes in the electron density of the electrode material. Recently, this method has been employed to probe redox activity, enabling the differentiation of charge storage mechanisms based on characteristic patterns in absorbance changes [27]. In EDL-type charge storage, the observed absorbance change remains relatively constant with respect to potential, reflecting continuous electronic changes. Pseudocapacitive processes typically exhibit a modest slope change in absorbance with respect to potential, indicating subtle potential-dependent redox activity. In contrast, battery-type mechanisms produce sharp and intense absorbance changes within a narrow potential range, associated with phase transitions [27].

To implement this approach, a custom three-electrode spectroelectrochemical cell was constructed, using a thin $Ti_3C_2T_x$ film spray-coated on a glass substrate as the working electrode, a thicker spray-coated $Ti_3C_2T_x$ film as the counter electrode, and an Ag wire as the reference electrode. Fig. 4a-c presents the full UV–Vis absorption spectra of $Ti_3C_2T_x$ during the cathodic scan. At OCP, a peak centered at 750 nm was observed, corresponding to the surface plasmon resonance of $Ti_3C_2T_x$. Upon cathodic polarization, a blueshift was observed in all electrolytes, indicative of increased electron density of Ti species.
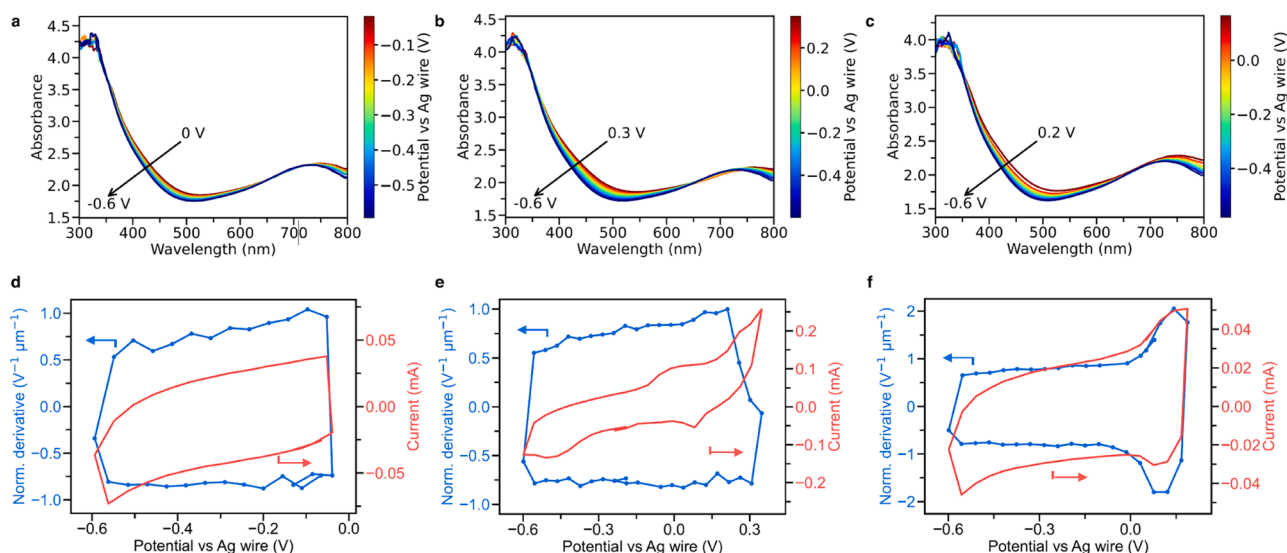
Fig. 4. Operando UV–Vis absorption spectra of Ti$_3$C$_2$T$_x$ MXene during cathodic scan at a scan rate of 1 mV s^{-1} in 2 M NaClO$_4$ dissolved in (a) H$_2$O, (b) 75 H$_2$O:25 ACN and (c) 50 H$_2$O:50 ACN. Electrochemical (in red) and UV–Vis absorbance derivative CV (in blue) curves of Ti$_3$C$_2$T$_x$ in 2 M NaClO$_4$ dissolved in (d) H$_2$O, (e) 75 H$_2$O:25 ACN and (f) 50 H$_2$O:50 ACN acquired at a scan rate of 1 mV s^{-1}.

Figure S7 shows the relative absorbance changes of the plasmonic peak at different potential. In both 2 M NaClO$_4$ H$_2$O and 75 H$_2$O:25 ACN, linear relative absorbance changes (normalized by film thickness and potential) were observed across the full voltage window with a slope of 0.82 V^{-1} μm^{-1} and 0.75 V^{-1} μm^{-1}, respectively. In contrast, an increase of the slope from 0.78 V^{-1} μm^{-1} to 1.89 V^{-1} μm^{-1} was seen in 50 H$_2$O:50 ACN under the redox potential (+0.1 V), suggesting that the additional process in 75 H$_2$O:25 ACN (S1) and 50 H$_2$O:50 ACN (S1') corresponds to different charge storage mechanism.

To better distinguish between EDL and pseudocapacitive behavior, we analyzed the potential-dependent derivative of absorbance at a characteristic wavelength at 450 nm, where the spectral response change was most significant. This approach provides a more direct view of redox activity change across different electrolytes [27]. In 2 M NaClO$_4$ H$_2$O, the absorbance derivative remained nearly constant at 0.8 V^{-1} μm^{-1} throughout the potential window (-1 V $-$ 0 V vs. Ag). This uniform response indicates that charge storage process is primarily non-Faradaic (Fig. 4d). In 75 H$_2$O:25 ACN, despite the presence of broad redox peaks with a large peak separation in the CV, the absorbance derivative exhibited a similar rectangular shape and magnitude as in H$_2$O, indicating minimal charge transfer (Fig. 4e). Similar characteristics have been reported in LiCl-based water-in-salt (WIS) electrolytes, where additional desolvation-free Li$^+$ intercalation at positive potential induces significant interlayer expansion with increased intersheet resistance [16]. Despite these structural and resistance changes, this desolvation-free Li$^+$ intercalation involves minimal Faradaic reaction [27]. In contrast, a different absorbance feature was seen in 50 H$_2$O:50 ACN electrolyte. The derivative curve resembles the shape of the CV curve, with a rectangular region (1.0 V^{-1} μm^{-1}) at negative potentials indicative of non-Faradaic behavior, and a pronounced peak (2.5 V^{-1} μm^{-1}) at the redox potentials, characteristic of a pseudocapacitive charge storage process (Fig. 4f).

2.3. Solvation structure evolution of NaClO$_4$ electrolytes with different ACN content

To understand the origin of different charge storage mechanisms in 2 M NaClO$_4$ with varying ACN content, we first examined the evolution of the Na$^+$ solvation structure using NMR and FTIR spectroscopy. As shown in Fig. 5a, the ^{1}H NMR signal of water progressively shifts upfield from 3.82 ppm in 2 M NaClO$_4$ H$_2$O to 3.71 ppm in 75 H$_2$O:25 ACN, 3.45 ppm

in 50 H$_2$O:50 ACN, and 3.19 ppm in 25 H$_2$O:75 ACN. This trend suggests disruption of the water-water hydrogen bonding network by enhanced interactions between H$_2$O and ACN [28]. FTIR analysis of the $-$-OH stretching region (Fig. 5b) corroborates this trend, showing an increasing contribution of the weak hydrogen bonding ($\sim$ 3620 cm^{-1}) as the ACN content rises [29]. Meanwhile, the C$\equiv$N stretching vibration band of ACN shows a redshift from 2258.8 cm^{-1} in 75 H$_2$O:25 ACN to 2256.7 cm^{-1} in 25 H$_2$O:75 ACN (Fig. 5d). This redshift could arise either from strengthened dipolar interactions between ACN and water molecules or from the enhanced ion-dipole interactions between ACN and Na$^+$ ions. However, the complex shift trend observed in the ^{1}H NMR spectra of ACN suggests that the latter scenario dominates. The ^{1}H NMR signal of ACN (Fig. 5c) initially shifts slightly upfield from 1.73 ppm in 75 H$_2$O:25 ACN to 1.71 ppm in 50 H$_2$O:50 ACN, followed by a pronounced downfield shift to 1.90 ppm in 25 H$_2$O:75 ACN. This trend reflects the evolving role of ACN in the Na$^+$ solvation. At lower ACN content, ACN molecules primarily interact with water through dipole-dipole interaction, while Na$^+$ ions remain predominantly solvated by water molecules (Fig. 5g, middle), resulting in the initial upfield shift. As the ACN content increases to 50 %, stronger coordination between Na$^+$ and ACN induces deshielding of ACN protons, causing a noticeable downfield shift in the ^{1}H NMR signal when comparing 25 H$_2$O:75 ACN to 50 H$_2$O:50 ACN.

Further insight on Na$^+$ ion solvation is provided by ^{23}Na NMR (Fig. 5e), which shows a continuous upfield shift from -1.48 ppm in H$_2$O to -1.73 ppm in 75 H$_2$O:25 ACN, -2.83 ppm in 50 H$_2$O:50 ACN, and -3.18 ppm in 25 H$_2$O: 75ACN. This reflects increased shielding of Na$^+$ nuclei, as more ACN molecules and ClO$_4^-$ coordinate with Na$^+$ ions and weaken the interaction between Na$^+$and water (Fig. 5g, right). FTIR spectra in the ClO$_4^-$ stretching region (Fig. 5f) reveals a redshift of the asymmetric ClO$_4^-$ band and new vibrational features which may be associated with contact ion pair formation around 1038 cm^{-1}, supporting increased Na$^+$-ClO$_4^-$ interactions at high ACN content [30,31].

2.4. Potential-dependent Na$^+$ intercalation with different solvation level enabled by ACN-containing electrolytes

The dominant charge storage mechanism in MXenes, either through non-Faradaic or surface-redox reaction, is influenced by ion desolvation prior to ion intercalation [8,9]. This desolvation process is strongly affected by the surface terminations of the MXenes and the composition
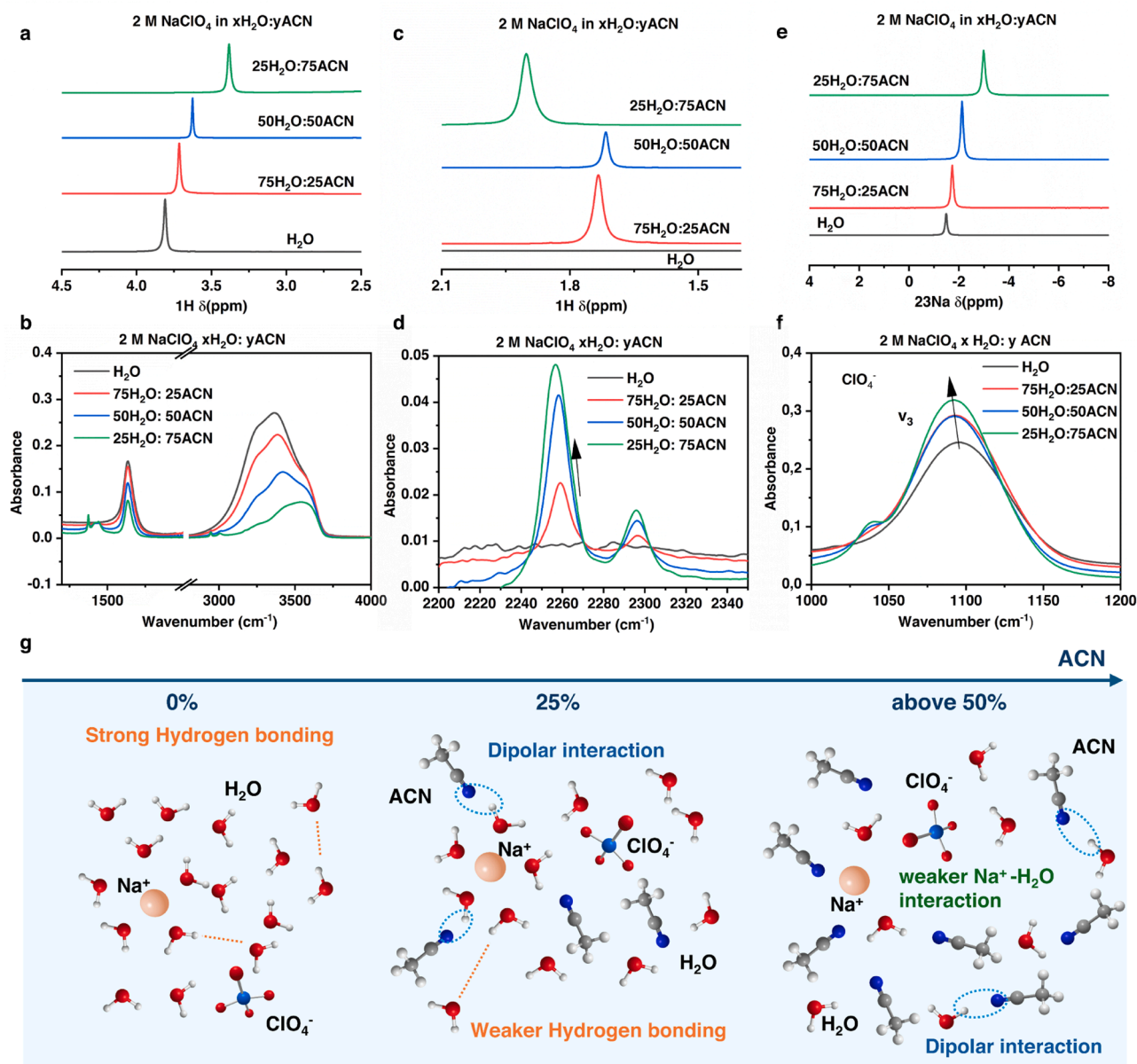
Fig. 5. Ion Solvation structure in different electrolytes. (a) ^{1}H NMR and (b) FTIR spectra of water. (c) ^{1}H NMR and (d) FTIR spectra of ACN. (e) ^{23}Na NMR spectra. (f) FTIR spectra of ClO_4^- in 2 M $NaClO_4$ H_2O, 75 H_2O:25 ACN and 50 H_2O:50 ACN. (g) Schematic illustration showing evolution of Na^+ ion solvation structure with increased ACN ratio. Red sphere: O atom; White sphere: H atom; Grey sphere: C atom; Blue sphere: Cl atom; Cyon sphere: N atom; Orange sphere: Na^+ cation.

of the electrolytes. Surface terminations directly affect the ion-surface interactions and interlayer spacing, which govern how easily ions can shed their solvation shells when entering the interlayer [32,33]. On the other hand, adjusting the electrolyte composition alters the solvation structure in the bulk electrolyte and the interaction with electrodes, which in turn affect the desolvation energy and subsequent ion intercalation behavior [15,34,35]. Since direct ion-surface contact is a prerequisite for efficient charge transfer, the degree and nature of ion intercalation can serve as an indirect probe of the underlying charge storage mechanism [9]. Therefore, to correlate ion solvation with tunable charge storage behavior across different ACN ratios, it is essential to investigate how ion intercalation evolves in different electrolytes. To this end, operando XRD was employed to monitor the structural evolution of $Ti_3C_2T_x$ electrodes during electrochemical cycling under varying solvation conditions.

Fig. 6**a-c** show the d-spacing evolution of (0 0 2) plane of $Ti_3C_2T_x$. Upon immersion in the electrolytes, large d-spacing of approximately

16.08 Å, 16.35 Å, and 16.44 Å was observed for 2 M $NaClO_4$ in H_2O, 75 H_2O:25 ACN, and 50 H_2O:50 ACN, respectively, due to spontaneous co-intercalation of Na^+ with different solvent molecules (**Figure S8**). The spontaneous intercalation of Na^+ ions was further confirmed by X-ray photoelectron spectroscopy (XPS), which indicated approximately 0.06–0.08 Na^+ ions per $Ti_3C_2T_x$ unit (**Figure S9, Table S1**). Moreover, FTIR spectroscopy on $Ti_3C_2T_x$ after electrolyte immersion and high-vacuum drying (10^{-7} mbar) revealed a broad O—H stretching band at 3426 cm^{-1} in 2 M $NaClO_4$ H_2O and 75 H_2O:25 ACN, strongly suggesting the confined water molecules in the interlayer (**Figure S10**)[36]. This peak shows a blueshift to 3445 cm^{-1} in 50 H_2O:50 ACN, suggesting weaker hydrogen bonding remained in MXene's interlayer. Additionally, the vibrational band corresponding to dangling −OH on the MXene surface at 3622 cm^{-1} was more pronounced in 50 H_2O: 50 ACN. Noteworthy, during the first cathodic scan, no distinct reduction peak is observed in any of the electrolytes (**Figure S11**), while operando XRD reveals a gradual decrease in interlayer spacing, reaching 15.45 Å, 16.14
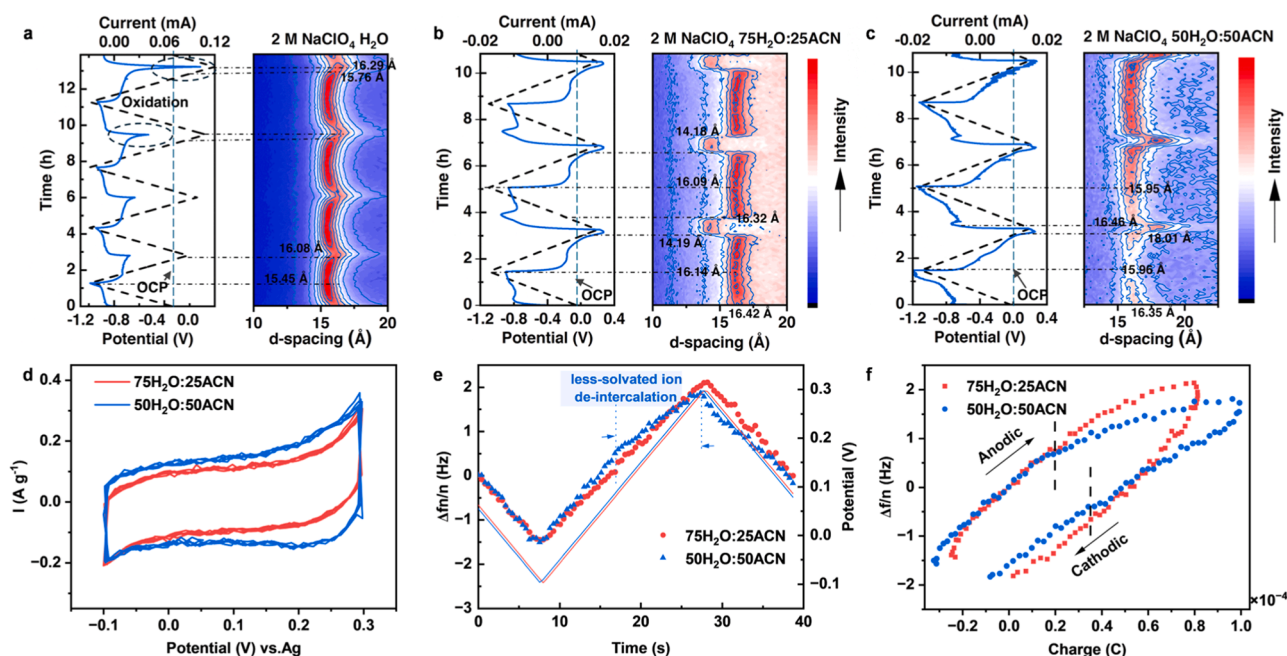
Fig. 6. Operando XRD and EQCM measurements of $Ti_3C_2T_x$ MXene in 2 M $NaClO_4$ electrolytes with different solvent compositions during cycling. Current-voltage curve and corresponding XRD contour plots during the first three electrochemical cycles in 2 M NaClO4 (a) H_2O and (b) 75 H_2O:25 ACN. (c) 50 H_2O:50 ACN. (d) CV curve collected at 20 mV s^{-1} using EQCM cell. (e) Frequency change (f_n/n) during the 1st cycle. (f) Frequency change (f_n/n)-charge (q) in 75 H_2O:25 ACN and 50 H_2O:50 ACN.

Å, and 15.96 Å at −1.1 V in H_2O, 75 H_2O:25 ACN, and 50 H_2O:50 ACN respectively (Fig. 6**a-c**). These moderate decreases (by 0.6 Å, 0.21 Å, and 0.48 Å) suggested the electrochemical intercalation of partially desolvated Na^+ ions into MXene interlayers at negative potential, driven by electrostatic attraction between Na^+ and negatively charged $Ti_3C_2T_x$ [37]. However, different structural evolution emerged in different electrolytes during the subsequent anodic scan. In 2 M $NaClO_4$ H_2O, the *d*-spacing increased gradually from 15.45 Å at −1.1 V to 16.08 Å at 0 V, attributed to the de-intercalation of partially desolvated Na^+ ions (Fig. 6**a**). In contrast, a two-step de-intercalation process was evident in ACN-containing electrolytes: a subtle, continuous interlayer spacing change at negative potential and a sharp and substantial interlayer spacing change at more positive potential above open-circuit potential (OCP).

Upon the first anodic sweep in 75 H_2O:25 ACN, the *d*-spacing of $Ti_3C_2T_x$ initially increased slightly from 16.14 Å to 16.32 Å as the potential rose from −1.1 V to −0.05 V, followed by an abrupt contraction to 14.19 Å at −0.05 V (Fig. 6**b**). The initial gradual expansion is likely due to the de-intercalation of partially desolvated Na^+ ions. While the subsequent sharp shrinkage by ~2.1 Å is potentially attributed to the electrochemical de-intercalation of strongly solvated Na^+-H_2O clusters. These Na^+-solvent clusters were spontaneously pre-inserted upon immersion and remained in the interlayer during the initial cathodic scan. Once the applied potential exceeded the OCP, the positive bias triggered the de-insertion of Na^+ along with coordinated solvent molecules, resulting in a pronounced reduction in interlayer spacing. This was supported by a control CV experiment where the first sweep was initiated in the positive direction, from OCP to 0.2 V, effectively avoiding any electrochemical Na^+ intercalation (**Figure S12**). The observation of a clear anodic peak further suggests that the origin of the anodic peak arises from de-intercalation of the pre-inserted Na^+ ions.

To further investigate whether ACN co-solvents accompanied Na^+ during de-intercalation, supplementary measurements were performed in 2 M $NaClO_4$ 75 H_2O:25 DMF. DMF was selected due to its larger molecular size and higher donor number, while the latter factor results in stronger coordination with Na^+ ions. If organic cosolvents were de-inserted together with Na^+ ions, the larger size of DMF would be

expected to cause a noticeable difference in the degree of *d*-spacing contraction compared to ACN. However, a similar *d*-spacing contraction of ~2.0 Å was observed (**Figure S13**), suggesting that Na^+ ions were primarily de-inserted together with water molecules. This indicates that organic cosolvents did not directly participate in de-intercalation but instead modified the Na^+-H_2O coordination, as evidenced by FTIR and NMR. Such modulation of the Na^+-H_2O interaction is necessary to enable electrochemical de-intercalation. Supporting this, applying a potential of +0.2 V in 2 M $NaClO_4$ H_2O only led to severe oxidation with a minor *d*-spacing increase of ~0.2 Å (Fig. 6**a**). During the subsequent cathodic sweep in 75 H_2O:25 ACN, the *d*-spacing abruptly expanded from 14.19 Å to 16.32 Å when the potential reached the reduction peak potential (−0.15 V), corresponding to the electrochemical intercalation of Na^+-H_2O cluster (Fig. 6**b**). This was followed by gradual contraction to 16.09 Å until −1.1 V, as partially desolvated Na^+ ions were inserted, confirming a reversible two-step electrochemical intercalation behavior. Despite the substantial *d*-spacing change upon charging/discharging, $Ti_3C_2T_x$ exhibited moderate long-term stability, retaining 79.1 % of its initial capacitance after 1 000 cycles at 1 A g^{-1} in 75 H_2O:25 ACN electrolyte (**Figure S14**).

A similar two-step (de-)intercalation behavior was also observed in the 50 H_2O:50 ACN system, albeit with different trends (Fig. 6**c**). Starting from the fully intercalated state at −1.1 V, the *d*spacing gradually increased from 15.96 Å to 16.35 Å as the potential swept anodically toward 0 V. Upon reaching 0 V, a sharp increase in *d*-spacing to 18.01 Å (~1.7 Å jump) was observed near the oxidation peak. Although FTIR and NMR analyses suggest enhanced coordination between ClO_4^- anion and Na^+ ions with increased ACN ratios, direct intercalation of anions into MXene interlayers is energetically unfavorable [30]. The influence of the counter anion was further investigated by conducting operando XRD in 2 M NaCl 75 H_2O:25 ACN within the positive potential range. Despite the stronger Na^+-Cl^- coordination, a similar electrochemical response was observed in NaCl 75 H_2O:25 ACN, such that noticeable redox peaks at positive potentials appeared. Moreover, operando XRD revealed a comparable ~2 Å contraction in *d*-spacing at the anodic peak potential (**Figure S15**). These results demonstrate that the high-potential intercalation process is dominated by Na^+-solvent

interactions, and that Cl⁻ does not intercalate into the MXene. However, the identity of the anion influences electrolyte solubility in mixed solvents. Notably, NaCl does not fully dissolve in 50 H$_2$O:50 ACN, preventing direct comparison under this condition.

Therefore, the observed expansion in *d*-spacing in 50 H$_2$O:50 ACN is likely attributed to the de-intercalation of weakly solvated Na⁺ ions, which strongly interact with the negatively charged MXene surfaces and help maintain a compact interlayer structure. Removal of these Na⁺ ions may reduce electrostatic attraction with MXene layer, allowing the residual confined solvent molecules to reorient or redistribute more freely, resulting in a looser molecular packing and expanded interlayer spacing. During the subsequent cathodic scan, the *d*-spacing abruptly reduced to 16.46 Å at the cathodic peak potential, indicating reversible insertion of weakly solvated Na⁺ ions and re-establishment of compact interlayer structure. If a greater number of Na⁺ ions or strongly solvated Na⁺ species were intercalated, interionic repulsion or steric effects would likely lead to interlayer expansion instead. Further evidence for the participation of weakly solvated Na⁺ species is provided by electrochemical quartz crystal microbalance with dissipation monitoring (EQCM-D) analysis. As shown in Fig. S16, the dissipation change (ΔD) remains negligible across the entire voltage window, confirming that the frequency shifts arise predominantly from gravimetric mass changes rather than viscoelastic effects of the Ti$_3$C$_2$T$_x$ film. The corresponding frequency(Δf)-voltage(*V*)-time(*t*) (Fig. 6e) and frequency (Δf)-charge(*q*) (Fig. 6f) profiles further reveal the ion intercalation process. In 50 H$_2$O:50 ACN electrolytes, the frequency change slows when the potential reaches ~0.1 V (Fig. 6e), which coincides with the anodic peak potential in the CV (Fig. 6d). Moreover, the Δf-*q* plot exhibits a reduction in slope at higher state of charge (Fig. 6f). This behavior signifies the insertion/extraction of species with lower effective molar masses at higher potentials. Quantitative analysis using the Sauerbrey relation coupled with Faraday's law yields water coordination numbers of only ~1–3 per Na⁺ at higher potentials (from +0.1 V above) (**Table S2**), in contrast to the strongly hydrated species at lower potential (~3–5 H$_2$O per Na⁺). Together, these results directly support the mechanism of weakly solvated Na⁺ (de)intercalation driving the distinct charge storage behavior observed in 50 H$_2$O:50 ACN.

In summary, the incorporation of ACN into the electrolyte alters the solvation structure of Na⁺ ions, thereby modulating the intercalation behavior and charge storage mechanisms of Ti$_3$C$_2$T$_x$ MXene. This solvation structure modification activates a two-step Na⁺ intercalation process in Ti$_3$C$_2$T$_x$ MXene upon cathodic sweep. At higher potential (S1 & S1'), sharp interlayer spacing changes are observed near the cathodic peak when ACN is employed as the cosolvent. In 75 H$_2$O:25 ACN, the interlayer spacing expands abruptly by 2.1 Å at high potential, indicating the intercalation of strongly solvated Na⁺-H$_2$O clusters. While this step does not contribute to significant charge transfer, it enables additional ion storage with rapid kinetics (Fig. 1, middle). This intercalation behavior leads to an overall ~30 % increase in capacitance and improved rate performance compared to pure water. In contrast, in 50 H$_2$O:50 ACN, Ti$_3$C$_2$T$_x$ undergoes an abrupt contraction in *d*-spacing by 1.6 Å, likely due to the intercalation of weakly solvated Na⁺ ions and the solvent reorganization, accompanied by enhanced redox activity (Fig. 1, right). At more negative potential (S2), both systems involve the intercalation of partially desolvated Na⁺ ions. This behavior is consistent with that observed in pure aqueous electrolytes and is non-Faradaic in nature (Fig. 1, left).

3. Conclusion

This study demonstrates that modifying the electrolyte composition by introducing ACN as co-solvent alters the Na⁺ solvation structure and thus the charge storage behavior in Ti$_3$C$_2$T$_x$ MXene. As Na⁺-H$_2$O interactions weaken with ACN addition, a distinct high-potential intercalation step emerges alongside the conventional low-potential EDL process. Importantly, we show that the nature of this additional

intercalation step, whether non-Faradaic or pseudocapacitive, is correlated to the solvent-ion interactions. These findings establish a clear relationship between ion solvation and intercalation behavior in MXenes, offering a practical approach to enhance both capacitance and rate capability through electrolyte design. Extending such co-solvent strategies to other ion-electrode systems may provide a rational pathway to optimize electrochemical performance through controlled ion-solvent interactions.

4. Methods

Synthesis of Ti$_3$C$_2$T$_x$: To synthesize Ti$_3$C$_2$T$_x$, 1 g Ti$_3$AlC$_2$ was gradually added into a solution of 1.6 g LiF and 20 ml of 9 M HCl. This mixture was kept at 35 °C and stirred for 24 h for etching. Subsequently, the etched material was washed several times with deionized water through centrifugation at 8000 rpm until the pH of the supernatant was neutralized to 6. The remaining sediment was re-dispersed in 40 ml of deionized water and subjected to 1 hour of sonication under an argon atmosphere to facilitate the delamination of the multilayers. The suspension was then centrifuged at 3500 rpm for 1 h, and the black supernatant was collected, yielding a few-layered Ti$_3$C$_2$T$_x$ colloidal solution. The Ti$_3$C$_2$T$_x$ film was then obtained through vacuum-assisted filtration and stored in a desiccator before subsequent characterization.

Electrochemical measurements: Electrochemical performance was evaluated using Swagelok cells configured in a three-electrode setup with a Biologic VSP-300 potentiostat. In this configuration, the free-standing Ti$_3$C$_2$T$_x$ films served as the working electrode, an Ag wire and activated carbon were used as the reference and counter electrode, respectively, while Whatman GF-A films served as separators. Cyclic voltammetry was conducted over scan rates ranging from 5 mV s⁻¹ to 1 V s⁻¹. For galvanostatic charge and discharge (GCD) tests, current densities varied from 0.2 A g⁻¹ to 10 A g⁻¹. Electrochemical impedance spectroscopy was performed with a 10 mV amplitude across a frequency range from 10 mHz to 200 kHz. The gravimetric specific capacitance derived from cyclic voltammetry is calculated using the formula:

$$C\left(\text{F g}^{-1}\right) = \frac{\int i\,dv}{m\,s\,\Delta V}$$

where *i* represents the current (A), *s* is the scan rate (V s⁻¹), *m* is the mass of the working electrode (g), and ΔV is the applied voltage window (V).

Material characterization: X-ray diffraction (XRD) analysis was performed using a PANalytical X'Pert Pro diffractometer with Cu K$_\alpha$ radiation ($\lambda = 0.1542$ nm) at an operating voltage of 45 kV and a current of 40 mA. Operando XRD patterns were obtained over a 2θ range of $3°-15°$ with a step size of $0.02°$ and a scan rate of $2.5°$/min. These measurements were conducted simultaneously with CV at a scan rate of 0.2 mV s⁻¹, using a Biologic VSP-300 potentiostat. Cross-sectional scanning electron microscopy (SEM) was performed with JEOL JSM-6010LA equipment. NMR spectra were acquired using a Bruker 600 MHz (14.1 T) Ascend magnet equipped with a NEO console. For NMR measurements, NaClO$_4$ salts were dissolved in a mixture of deuterated water (D$_2$O) and ACN in different volume ratio. The Larmor frequencies were 600.13 MHz for ¹H and 158.76 MHz for ²³Na. The 90° pulse lengths were determined to be 16.2 μs for ¹H and 13.4 μs for ²³Na. Spectra were recorded using a 30° excitation pulse with a 2 s recycle delay, collecting 4 scans for ¹H and 8 scans for ²³Na. A 2 M NaCl solution in D$_2$O served as the reference for ²³Na, while tetramethylsilane (TMS), sealed in a capillary and immersed in the electrolyte, was used as the ¹H reference. Fourier-transform infrared (FTIR) spectroscopy was employed to analyze the solvation structure of electrolytes using a Thermo Scientific Nicolet iS50 spectrometer equipped with an iS50 ATR module. X-ray photoelectron spectroscopy measurements were performed on a Thermo Scientific K-Alpha Spectrometer with an Al K-alpha (1486.6 eV) monochromator. The spot diameter was set to 400 μm. Survey spectra were recorded with a pass energy of 200 eV and step size of 0.5 eV, while

high-resolution spectra were recorded with a pass energy of 50 eV and step size of 0.1 eV. The binding energies were referenced to adventitious carbon at 284.8 eV. To minimize local heterogeneity, survey spectra were collected from three randomly selected spots on each sample, and the averaged values were used for quantification. The Na1s and Ti2p peak areas were integrated and corrected with the instrument's relative sensitivity factors (RSFs) to determine atomic percentages. Since $Ti_3C_2T_x$ contains three Ti atoms per formula unit, the average Na^+ content was obtained by normalizing the measured Na:Ti ratio to three Ti atoms.

EQCM-D experiments were carried out using a Bionaivis QCM-D 100 equipped with a temperature control unit. Frequency and dissipation at different states of charge were recorded by applying CV at 20 mV s^{-1} using a Biologic potentiostat in a three-electrode configuration. A thin $Ti_3C_2T_x$ layer ($\sim$20 µg cm^{-2}) was spray coated onto a Ti/Au-plated 14 mm quartz crystal, which served as the working electrode. Ti foil and Ag wire were used as the counter and reference electrodes, respectively. A narrow potential window between -0.1 V and 0.3 V vs. Ag was applied to avoid potential side reactions. The effective molar mass of the (de) intercalated species was extracted using the Sauerbrey equation combined with Faraday's law:

$$M = \frac{C_f q}{nF}$$

where M is the atomic mass of the inserted species, q is the charge, n is the number of electrons transferred, F is the Faraday constant, and C_f is the mass sensitivity constant of the sensor ($C_f = 56.6$ Hz µg^{-1} cm^{-2}). From this, the average number of coordinated water molecules per Na^+ ion can be estimated.

Operando UV–Vis spectroscopy was performed using a Thermo Scientific Pro Evolution One Plus spectrophotometer, equipped with a xenon flash lamp as the light source. The system was operated with a spectral bandwidth of 1 nm and a beam size of 0.46 mm $\times$ 2.5 mm. Thin $Ti_3C_2T_x$ working electrodes and thick $Ti_3C_2T_x$ counter electrodes were prepared by spray-coating a $\sim$5 mg mL^{-1} $Ti_3C_2T_x$ aqueous dispersion onto pre-cleaned glass substrates at 60 °C. The thicker counter electrode ensured sufficient capacitance to avoid polarization throughout the applied potential window, thereby preventing potential side reactions. Prior to measurement, a reference spectrum was acquired using a clean glass-glass configuration without electrolyte. The absorbance of the as-prepared electrode was recorded across 300–800 nm to estimate film thickness and serve as the initial baseline. Using a previously reported linear relation ($A = 0.005 \times l$), where A is the absorbance and l is the thickness of the $Ti_3C_2T_x$ working electrode [38]. The thicknesses were calculated for absorbance minima ranging from 0.6 to 1.8, corresponding to 120–360 nm, allowing us to obtain the normalized absorption. While this relation was originally validated for thinner coatings (5–70 nm), its consistent application across all samples allows for comparative analysis within this study. Subsequently, the in-situ cell was filled with electrolytes and sealed with UV-curable resin to prevent electrolyte evaporation and aligned in the beam path. Then the UV–Vis spectra were collected simultaneously with cyclic voltammetry. Under the scan mode, full absorbance spectra were captured every $\sim$ 45 mV by synchronizing with a 1 mV s^{-1} CV scan. To visualize spectral evolution, absorbance curves at selected potentials during anodic and cathodic sweeps were extracted. For quantitative evaluation, the fixed wavelength mode was used by monitoring a single wavelength (450 nm), which corresponds to the wavelength with the most pronounced optical response, was collected as a function of potential. The normalized absorbance derivative was calculated using the following equation: Normalized absorbance derivative $= (A_V - A_{V-\mathrm{d}V}) / (\mathrm{d}V \times l)$, where A_V is the absorbance at potential V, $\mathrm{d}V$ is the potential difference between measurement points, l is the thickness of the $Ti_3C_2T_x$ working electrode. This normalization accounts for both the potential scan resolution and film thickness, enabling direct comparison of optical behavior across different electrolyte systems.

CRediT authorship contribution statement

Chaofan Chen: Writing – review & editing, Writing – original draft, Visualization, Validation, Methodology, Investigation, Formal analysis, Data curation. **Albert de Kogel:** Writing – review & editing, Investigation, Formal analysis, Data curation. **Luca Bikker:** Writing – review & editing, Visualization, Investigation. **Pranav Karanth:** Writing – review & editing, Investigation. **Hao Wang:** Writing – review & editing, Investigation. **Swapna Ganapathy:** Writing – review & editing, Methodology, Investigation. **Marnix Wagemaker:** Writing – review & editing, Supervision, Resources, Funding acquisition. **Xuehang Wang:** Writing – review & editing, Supervision, Resources, Project administration, Funding acquisition, Conceptualization.

Declaration of competing interest

The authors declare that they have no known competing financial interests or personal relationships that could have appeared to influence the work reported in this paper.

Acknowledgments

Supplementary materials

Supplementary material associated with this article can be found, in the online version, at doi:10.1016/j.ensm.2025.104806.

Data availability

Data will be made available on request.

References

[1] N. Kittner, F. Lill, D. Kammen, Energy Storage Deployment and Innovation for the Clean Energy Transition, Nat. Energy 2 (2017) 17125.

[2] Y. Liu, Y. Zhu, Y. Cui, Challenges and Opportunities towards Fast-charging Battery Materials, Nat. Energy 4 (2019) 540–550.

[3] S. Fleischmann, J.B. Mitchell, R. Wang, C. Zhan, D. Jiang, V. Presser, V. Augustyn, Pseudocapacitance: From Fundamental Understanding to High Power Energy Storage Materials, Chem. Rev. 120 (2020) 6738.

[4] M. Naguib, V.N. Mochalin, M.W. Barsoum, Y. Gogotsi, 25th Anniversary Article: MXenes: A New Family of Two-Dimensional Materials, Adv. Mater. 26 (2014) 992.

[5] M.R. Lukatskaya, S. Kota, Z. Lin, M.-Q. Zhao, N. Shpigel, M.D. Levi, J. Halim, P.-L. Taberna, M.W. Barsoum, P. Simon, Y. Gogotsi, Ultra-high-rate Pseudocapacitive Energy Storage in Two-dimensional Transition Metal Carbides, Nat. Energy 2 (2017) 17105.

[6] X. Li, Z. Huang, C.E. Shuck, G. Liang, Y. Gogotsi, C. Zhi, MXene Chemistry, Electrochemistry and Energy Storage Applications, Nat. Rev. Chem. 6 (2022) 389.

[7] D. Chao, W. Zhou, F. Xie, C. Ye, H. Li, M. Jaroniec, S. Qiao, Roadmap for Advanced Aqueous Batteries: From Design of Materials to Applications, Sci. Adv 6 (2020) eaba4098.

[8] M. Okubo, A. Sugahara, S. Kajiyama, A. Yamada, MXene as a Charge Storage Host, Acc. Chem. Res. 51 (2018) 591.

[9] Y. Ando, M. Okubo, A. Yamada, M. Otani, Capacitive versus Pseudocapacitive Storage in MXene, Adv. Funct. Mater. 30 (2020) 2000820.

[10] Q. Gao, W. Sun, P. Ilani-Kashkouli, A. Tselev, P.R.C. Kent, N. Kabengi, M. Naguib, M. Alhabeb, W.-Y. Tsai, A.P. Baddorf, J. Huang, S. Jesse, Y. Gogotsi, N. Balke, Tracking Ion Intercalation into Layered Ti_3C_2 MXene Films across Length Scales, Energy Environ. Sci. 13 (2020) 2549.

[11] F. Ming, Y. Zhu, G. Huang, A. Emwas, H. Liang, Y. Cui, H. Alshareef, Co-Solvent Electrolyte Engineering for Stable Anode-Free Zinc Metal Batteries, J. Am. Chem. Soc. 144 (2022) 7160.

[12] L. Suo, O. Borodin, T. Gao, M. Olguin, J. Ho, X. Fan, C. Luo, C. Wang, K. Xu, Water-in-salt" Electrolyte Enables High-voltage Aqueous Lithium-ion Chemistries, Science 350 (2015) 938.

[13] J. Xie, Z. Liang, Y.-C. Lu, Molecular Crowding Electrolytes for High-voltage Aqueous Batteries, Nat. Mater 19 (2020) 1006.

[14] D. Chao, S. Qiao, Toward High-Voltage Aqueous Batteries: Super- or Low-Concentrated Electrolyte? Joule 4 (2020) 1846.

[15] X. Wang, T.S. Mathis, K. Li, Z. Lin, L. Vlcek, T. Torita, N.C. Osti, C. Hatter, P. Urbankowski, A. Sarycheva, M. Tyagi, E. Mamontov, P. Simon, Y. Gogotsi, Influences from Solvents on Charge Storage in Titanium Carbide MXenes, Nat. Energy 4 (2019) 241.

[16] A. Perju, D. Zhang, R.J. Wang, P.-L. Taberna, Y. Gogotsi, P. Simon, Operando Tracking of Resistance, Thickness, and Mass of $Ti_3C_2T_x$ MXene in Water-in-Salt, Electrolyte, Adv. Energy Mater. 15 (2025) 2405028.

[17] C. Chen, A. de Kogel, M. Weijers, L.J. Bannenberg, X. Wang, Enhancing Pseudocapacitive Intercalation in $Ti_3C_2T_x$ MXene with Molecular Crowding Electrolytes, 2D Mater. 11 (2023) 015001.

[18] X. Wang, T.S. Mathis, Y. Sun, W.-Y. Tsai, N. Shpigel, H. Shao, D. Zhang, K. Hantanasirisakul, F. Malchik, N. Balke, D. Jiang, P. Simon, Y. Gogotsi, Titanium Carbide MXene Shows an Electrochemical Anomaly in Water-in-Salt Electrolytes, ACS. Nano 15 (2021) 15274.

[19] R.J. Sengwa, P. Dhatarwal, S. Choudhary, Static Permittivities, Viscosities, Refractive Indices and Electrical Conductivities of the Binary Mixtures of Acetonitrile with Poly(ethylene glycol)-200 at Temperatures 288.15–318.15 K, J. Mol. Liq. 271 (2018) 128.

[20] Y. Sun, Y. Wang, L. Liu, B. Liu, Q. Zhang, D. Wu, H. Zhang, X. Yan, Towards the Understanding of Acetonitrile Suppressing Salt Precipitation Mechanism in a Water-in-salt Electrolyte for Low-temperature Supercapacitors, J. Mater. Chem. A 8 (2020) 17998.

[21] J. Chen, J. Vatamanu, L. Xing, O. Borodin, H. Chen, X. Guan, X. Liu, K. Xu, W. Li, Improving Electrochemical Stability and Low-Temperature Performance with Water/Acetonitrile Hybrid Electrolytes, Adv. Energy Mater. 10 (2020) 1902654.

[22] Q. Dou, S. Lei, D.-W. Wang, Q. Zhang, D. Xiao, H. Guo, A. Wang, H. Yang, Y. Li, S. Shi, X. Yan, Safe and High-rate Supercapacitors based on an "Acetonitrile/water in salt" Hybrid Electrolyte, Energy Environ. Sci. 11 (2018) 3212.

[23] J. Shi, K. Xia, L. Liu, C. Liu, Q. Zhang, L. Li, X. Zhou, J. Liang, Z. Tao, Ultrahigh Coulombic Efficiency and Long-life Aqueous Zn Anodes Enabled by Electrolyte Additive of Acetonitrile, Electrochim. Acta 358 (2020) 136937.

[24] S. Yadav, N. Kurra, Diffusion Kinetics of Ionic Charge Carriers across $Ti_3C_2T_x$ MXene-Aqueous Electrochemical Interfaces,, Energy Storage Mater. 65 (2024) 103094.

[25] J. Wang, J. Polleux, J. Lim, B. Dunn, Pseudocapacitive Contributions to Electrochemical Energy Storage in TiO_2 (Anatase) Nanoparticles, J. Phys. Chem. C 111 (2007) 14925.

[26] N.O. Laschuk, E.B. Easton, O.V. Zenkina, Reducing the Resistance for the use of Electrochemical Impedance Spectroscopy Analysis in Materials Chemistry, RSC. Adv. 11 (2021) 27925.

[27] D. Zhang, R. (John) Wang, X. Wang, Y. Gogotsi, In Situ Monitoring Redox Processes in Energy Storage Using UV–Vis Spectroscopy, Nat. Energy 8 (2023) 567.

[28] Y. Wang, T. Ou, Y. Dong, L. Chen, Y. Huang, D. Sun, W. Qiang, X. Pei, Y. Li, Y. Tan, A Green Asymmetric Bicyclic Co-Solvent Molecule for High-Voltage Aqueous Lithium-Ion Batteries, Adv. Mater. 36 (2024) 2311009.

[29] Z. Wu, Y. Li, A. Amardeep, Y. Shao, Y. Zhang, J. Zou, L. Wang, J. Xu, D. Kasprzak, E.J. Hansen, J. Liu, Unveiling the Mysteries: Acetonitrile's Dance with Weakly-Solvating Electrolytes in Shaping Gas Evolution and Electrochemical Performance of Zinc-ion Batteries, Angew. Chem 136 (2024) e202402206.

[30] J.S. Loring, W.R. Fawcett, Ion−Solvent Interactions in Acetonitrile Solutions of Lithium, Sodium, and Tetraethylammonium Perchlorate Using Attenuated Total Reflectance FTIR Spectroscopy, J. Phys. Chem. A 103 (1999) 3608.

[31] Y. Chen, Y.-H. Zhang, L.-J. Zhao, ATR-FTIR spectroscopic studies on aqueous $LiClO_4$, $NaClO_4$, and $Mg(ClO_4)_2$ solutions, Phys. Chem. Chem. Phys. 6 (2004) 537.

[32] Z. Bo, R. Wang, B. Wang, S. Sunny, Y. Zhao, K. Ge, K. Xu, Y. Song, E. Raymundo-Piñero, Z. Lin, H. Shao, Q. Yu, J. Yan, K. Cen, P.-L. Taberna, P. Simon, Ion Desolvation for Boosting the Charge Storage Performance in Ti_3C_2 MXene Electrode, Nat. Commun. 16 (2025) 3813.

[33] T. Zhang, L. Chang, X. Zhang, H. Wan, N. Liu, L. Zhou, X. Xiao, Simultaneously Tuning Interlayer Spacing and Termination of MXenes by Lewis-basic Halides, Nat. Commun. 13 (2022) 6731.

[34] G.A. Ferrero, G. Åvall, K. Janßen, Y. Son, Y. Kravets, Y. Sun, P. Adelhelm, Solvent Co-Intercalation Reactions for Batteries and Beyond, Chem. Rev. 125 (2025) 3401.

[35] M.L. Divya, Y.-S. Lee, V. Aravindan, Solvent Co-intercalation: An Emerging Mechanism in Li-, Na-, and K-Ion Capacitors, ACS. Energy Lett. 6 (2021) 4244.

[36] M. Lounasvuori, Y. Sun, T.S. Mathis, L. Puskar, U. Schade, D.-E. Jiang, Y. Gogotsi, T. Petit, Vibrational Signature of Hydrated Protons Confined in MXene Interlayers, Nat. Commun. 14 (2023) 1322.

[37] M.R. Lukatskaya, O. Mashtalir, C.E. Ren, Y. Dall'Agnese, P. Rozier, P.L. Taberna, M. Naguib, P. Simon, M.W. Barsoum, Y. Gogotsi, Cation Intercalation and High Volumetric Capacitance of Two-Dimensional Titanium Carbide, Science 341 (2013) 1502.

[38] K. Hantanasirisakul, M.-Q. Zhao, P. Urbankowski, J. Halim, B. Anasori, S. Kota, C. E. Ren, M.W. Barsoum, Y. Gogotsi, Fabrication of $Ti_3C_2T_x$ MXene Transparent Thin Films with Tunable Optoelectronic Properties, Adv. Electron. Mater. 2 (2016) 1600050.